Soft Matter

PAPER

View Article Online
View Journal | View Issue

Cite this: *Soft Matter*, 2020, **16**, 3425

Dispersing nano- and micro-sized portlandite particulates *via* electrosteric exclusion at short screening lengths†

Jason Timmons,‡[ab] Iman Mehdipour,‡[b] Shang Gao,[c] Hakan Atahan,[bd] Narayanan Neithalath,[e] Mathieu Bauchy,[fg] Edward Garboczi,[h] Samanvaya Srivastava *[cg] and Gaurav Sant*[abgi]

In spite of their high surface charge (zeta potential ζ = +34 mV), aqueous suspensions of portlandite (calcium hydroxide: $Ca(OH)_2$) exhibit a strong tendency to aggregate, and thereby present unstable suspensions. While a variety of commercial dispersants seek to modify the suspension stability and rheology (*e.g.*, yield stress, viscosity), it remains unclear how the performance of electrostatically and/or electrosterically based additives is affected in aqueous environments having either a high ionic strength and/or a pH close to the particle's isoelectric point (IEP). We show that the high native ionic strength (pH $\approx$ 12.6, IEP: pH $\approx$ 13) of saturated portlandite suspensions strongly screens electrostatic forces (Debye length: κ^{-1} = 1.2 nm). As a result, coulombic repulsion alone is insufficient to mitigate particle aggregation and affect rheology. However, a longer-range geometrical particle–particle exclusion that arises from electrosteric hindrance caused by the introduction of comb polyelectrolyte dispersants is very effective at altering the rheological properties and fractal structuring of suspensions. As a result, comb-like dispersants that stretch into the solvent reduce the suspension's yield stress by 5× at similar levels of adsorption as compared to linear dispersants, thus enhancing the critical solid loading (*i.e.*, at which jamming occurs) by 1.4×. Significantly, the behavior of diverse dispersants is found to be inherently related to the thickness of the adsorbed polymer layer on particle surfaces. These outcomes inform the design of dispersants for concentrated suspensions that present strong charge screening behavior.

Received 8th January 2020,
Accepted 15th March 2020

DOI: 10.1039/d0sm00045k

rsc.li/soft-matter-journal

[a] *Department of Materials Science and Engineering, University of California, Los Angeles, CA 90095, USA. E-mail: gsant@ucla.edu*
[b] *Laboratory for the Chemistry of Construction Materials (LC²), Department of Civil and Environmental Engineering, University of California, Los Angeles, CA 90095, USA*
[c] *Department of Chemical and Biomolecular Engineering, University of California, Los Angeles, CA 90095, USA. E-mail: samsri@ucla.edu*
[d] *Department of Civil Engineering, Istanbul Technical University, Istanbul, Turkey*
[e] *School of Sustainable Engineering and the Built Environment, Arizona State University, Tempe, AZ 86587, USA*
[f] *Laboratory for the Physics of Amorphous and Inorganic Solids (PARISlab), Department of Civil and Environmental Engineering, University of California, Los Angeles, CA 90095, USA*
[g] *Institute for Carbon Management, University of California, Los Angeles, CA 90095, USA*
[h] *Applied Chemicals and Materials Division, Material Measurement Laboratory, National Institute of Standards and Technology, Boulder, CO 80305, USA*
[i] *California Nanosystems Institute (CNSI), University of California, Los Angeles, CA 90095, USA*

† Electronic supplementary information (ESI) available: Particle size distribution, Fourier transform infrared spectroscopy, Lifshitz theory for calculation of the Hamaker constant, kinetic stability criterion, yield stress behavior for PCE-containing suspensions, fractal dimension of aggregates, crossover energy, nuclear magnetic resonance characterization. See DOI: 10.1039/d0sm00045k

‡ Both authors contributed equally to this work.

1. Introduction

The rheology of concentrated suspensions is important for many industrial processes. Colloidal dispersions and gels exhibit a wide range of rheological properties such as aging, shear thickening/thinning, and yielding. In particular, the yield stress and viscosity of suspensions greatly affects the processing of materials for diverse applications including cement and concrete pumping,[1,2] gel casting of ceramics,[3,4] and drug delivery,[5,6] as well as in emerging technologies such as particulate flow batteries,[7,8] and 3D-printing of slurries.[9,10] However, on account of their tendency to aggregate, the particles in a suspension may often organize into flocs, and settle, resulting in undesirable behavior including a reduction of the maximum (achievable) solid volume fraction (ϕ_{max}), and very high yield stress and viscosity that greatly complicate suspension processing.[11,12]

Generally, repulsive interactions between particles are introduced to enhance suspension stability by: introducing charges on the particle surfaces (electrostatic repulsion),[13,14] adsorbing or grafting

polymers onto particle surfaces to induce steric barriers,[15–17] and combinations thereof. However, even suspensions of strongly charged particles agglomerate readily, especially in aqueous environments that present either a high ionic strength and/or a pH close to the particle's isoelectric point (IEP). In such suspensions, strong screening of electrostatic forces results in a sharp increase in yield stress with particle loading.[18] As a result, the maximum achievable particle loadings (ϕ_{max}), *i.e.*, prior to the onset of jamming (*i.e.*, where flow is arrested and the suspension exhibits solid-like behavior) remain modest.

Polyelectrolyte dispersants are often used to impart electrosteric barriers to particle aggregation by forming an electrostatically adsorbed layer on particle surfaces that limits the closest approach distance between adjacent particles.[19] Thus, such dispersants act to reduce the yield stress while simultaneously enhancing the maximum particle loadings of dense stable suspensions. Steric barriers to particle aggregation are further accentuated by grafting non-ionic side chains onto the adsorbing polyelectrolyte backbones to form 'comb' polyelectrolytes.[20,21] The aqueous medium provides a good solvent for the side chains and they extend into the solution, increasing the distance of the closest approach between particles.

While commercially available dispersants are often effective in altering suspension stability and rheology, considerable challenges remain. For example, it remains difficult to design dispersants for suspensions that self-regulate their pH and have high ionic strengths.[22] This is especially important when dispersants interact with the solution resulting in aggregation that arises from ion bridging interactions and/or complexation between polymers and multivalent counterions (*e.g.*, Ca^{2+}).[23–25] Portlandite (*i.e.*, also known as slaked or hydrated lime or calcium hydroxide: $Ca(OH)_2$) is an example of such a solid, which in suspension, self-regulates its pH (*i.e.*, on account of its modest solubility; 20.3 mM at 25 °C,[26] I_m = 60.9 mM [molar ionic strength], and rapid dissolution rate). Portlandite suspensions find use in applications including: water treatment,[27–29] dental fillings,[30–32] food industry,[33,34] and construction materials.[35,36] On account of the relatively high ionic strength resulting from its dissolution that can screen electrostatic forces, portlandite often presents weakly-charged, unstable nanosized particulates in suspension. This is problematic in applications where the suspension is required to have both high particle volume fractions and amenable flow properties; their tendency to aggregate and the low value of ϕ_{max} make processing difficult.[11] Therefore, this study seeks to elucidate: (a) the mechanisms that affect the aggregation of portlandite suspensions, and (b) the interactions between $Ca(OH)_2$ suspensions and diverse dispersant chemistries that present varying stabilization mechanisms (*e.g.*, electrostatic and electrosteric), which produces varying dispersant layer thicknesses. Focus is placed on identifying the characteristics of polymeric dispersants that effectively improve the rheology of portlandite suspensions, and thereby offer guidelines for the design of new dispersants for industrial applications.

2. Materials and methods

2.1. Materials and sample preparation

Commercially available portlandite ($Ca(OH)_2$; Standard Hydrated Lime, Mississippi Lime Company)§ was used. It featured a purity of 94% ± 2% (by mass) with the remainder being composed of $CaCO_3$ as determined by thermogravimetric analysis (TGA; STA 6000, PerkinElmer). The particle size distribution of the portlandite was measured using static light scattering (SLS; LS13-320, Beckman Coulter), assuming a complex refractive index of 1.574 + 0.000i.[37] The particulates were dispersed using ultrasonication in isopropanol (IPA), which was used as the carrier fluid. The median particle diameter (d_{50}) of the particulates was estimated as 3.8 μm ± 0.2 μm (see ESI,† Fig. S1a). The density of the particulates was measured as 2235 kg m^{-3} ± 4 kg m^{-3} using helium pycnometry (AccuPyc II 1340, Micromeritics).

The morphology of the particles was examined using a field emission-scanning electron microscope (FEI NanoSEM 230). All SEM micrographs were acquired in secondary electron mode with a spot size of 4.0 nm, at an accelerating voltage of 10 kV, and a working distance of ≈5.5 mm. The particles form aggregates whose size is similar to that measured by static light scattering (see ESI,† Fig. S1b). Since light scattering is known to be ineffective in determining the primary particle size of the aggregated portlandite particulates,[11,35] transmission electron microscopy (TEM; FEI T12 Quick CryoEM and CryoET) was used to examine the primary particle size. A dilute suspension of portlandite particulates robustly dispersed (with the application of ultrasonication) in IPA was deposited on to a TEM grid; and the solvent was evaporated thereafter. Although large aggregates were still observed, the primary particle size was established as being on the order of 20-to-200 nm (see ESI,† Fig. S1c), as suggested previously.[11,35,36] However, it was not possible to meaningfully, on a statistical basis, resolve a sufficient number of non-agglomerated particles to establish a particle size distribution from the TEM imaging of the primary portlandite particles.

Three commercially available dispersants were used: (1) a polyacrylic acid-based dispersant (PAA, Acumer 9000, Dow Chemical), (2) a lignosulfonate-based dispersant (LS, MasterPolyheed 997, BASF Corporation), and (3) a poly-carboxylate ether-based dispersant (PCE, MasterGlenium 7500, BASF Corporation). The functional groups present in each polymer were qualitatively determined (see ESI,† Fig. S2) using Fourier transform infrared spectroscopy (FTIR; PerkinElmer Spectrum Two). In brief, LS contains sulfonic acid groups,[38] PAA contains carbonyl groups, and PCE contains carbonyl groups associated with its PAA backbone and ether groups corresponding to its polyethylene glycol (PEG) side chains [*N.B.*: the ratio between the abundance of carbonyl-to-ether groups is 0.09 : 1; mass basis].[39] The solids content of each additive was determined as 49.03 mass%, 45.01 mass%, and 26.59 mass%, respectively. The molecular weight of the polymeric dispersants is provided

§ Certain commercial equipment, software and/or materials are identified in this paper in order to adequately specify the experimental procedure. In no case does such identification imply recommendation or endorsement by the National Institute of Standards and Technology, nor does it imply that the equipment and/or materials used are necessarily the best available for the purpose.

Table 1 Properties and adsorption characteristics of the investigated dispersants

Dispersant type	Mass-average molecular weight, M_w (g mol^{-1})	Charge density at pH = 12 (eq. per mol)	Hydrodynamic radius, r_H (nm)	Adsorption capacity, $\rho_{a,m}$ ($g_{polymer}$ g_{solid}^{-1})	Binding affinity, K (~)
PCE	39 467	43.5	11.34	0.0325	43.32
PAA	6092	81.0	4.45	0.0305	229.7
LS	4050	8.4	2.61	0.0520	21.75

in Table 1. The dispersants were dosed at a level ranging between 0 mass% to 1.5 mass% of the total solid content in the suspension, including the solids content of the polymer dispersant.

In order to prevent any complications caused by the dissolution of portlandite, a previously saturated and filtered $Ca(OH)_2$ solution was used as the suspending fluid. Saturated $Ca(OH)_2$ solution was prepared by adding excess portlandite to deionized (DI) water, allowing for the solids to settle, and then filtering the solution using a 0.20 μm syringe filter. To produce suspensions, polymeric dispersants (when used) were added to the saturated $Ca(OH)_2$ solution, and then solid portlandite particulates were added to the solution. The mixtures were first mixed by hand, and then stirred for 120 s using a four-blade impeller-type high-shear mixer (RW 20 Digital, IKA) at 500 rpm to produce well-dispersed and homogenous suspensions with known particle volume fraction ϕ and dispersant dosage ρ (mass% of total solid, when used).

2.2. Experimental methods

2.2.1. Characterization of polymers

Molecular weight characterization. The molecular weight of the polymers was determined by aqueous gel permeation chromatography (GPC; Waters Alliance 2695 Separation Module) with a two-column setup (Shodex SB 804 HQ and Shodex SB 802.5 HQ). An evaporative light scattering detector (ELSD; Alltech 3300) analyzed the polymer after elution in the GPC columns. For quantitative analysis, external calibrations were carried out using narrow molecular weight polyethylene glycol (PEG) standards ranging from 400 g mol^{-1} to 150 000 g mol^{-1}.

Charge density characterization. The charge density of the polymers was determined by aqueous streaming current (Mütek PCD-05 Smart Particle Charge Detector) analyses. Each polymer was diluted to the range of 100 ppm to 1000 ppm and adjusted to pH = 12 by the addition of sodium hydroxide (NaOH). These samples were then titrated with 0.001 N poly-dimethyl-diallyl-ammonium chloride (polyDADMAC), until the streaming potential reached its isoelectric point (charge = 0 mV). Based on the amount of polyDADMAC added to neutralize the charge of each polymer, the charge density was calculated.

Dynamic light scattering. Dynamic light scattering (DLS) analysis (Malvern, Zetasizer Nano) was carried out to assess the hydrodynamic radius (*i.e.*, chain size: r_h, nm) of the three dispersants.

2.2.2. Characterization of portlandite suspensions

Zeta potential. To assess the electrokinetic interactions in the suspensions, the zeta potential (ζ, mV) was determined by measurement of electrophoretic mobilities using Phase Analysis Light Scattering (ZetaPALS, Brookhaven Instruments Corporation). The measurements were carried out on dilute portlandite suspensions (0.05 g_{solid} $L_{solution}^{-1}$) for a variety of dispersant dosages. In select circumstances, before the zeta potential was measured, the pH of the suspensions was adjusted to 12.8 and 13.0 by the addition of NaOH.

Suspension rheology. The rheological behavior of portlandite suspensions was assessed for a range of particle volume fractions (ϕ) and dispersant dosages using a combined motor-transducer rheometer (DHR-2, TA Instruments). A four-bladed vane-in-cup geometry was used, with a vane of 28 mm diameter and 42 mm height, and a cup of 30 mm diameter. For all measurements, the suspensions were conditioned to a temperature of 25 °C ± 0.1 °C. In general, two types of analyses were carried out:

• The apparent yield stress (σ_y) and shear rate ($\dot{\gamma}$)-dependent viscosity (η) were determined *via* a shear rate sweep. The apparent yield stress (σ_y) was identified as the stress plateau at lower shear rates ($\dot{\gamma} < 1$ s^{-1}).[40–42] Before the sweep, a 60 s pre-shear at $\dot{\gamma} = 100$ s^{-1} was performed to remove any shear history effects, followed by a 60 s rest period.[40,43,44] Different rest periods of up to 180 s were tested during preliminary experiments with no significant change (*i.e.*, less than 15% change in the peak stress stress) beyond 60 s of rest. As the measured yield stress does not fully correspond to the static yield stress when no sufficient rest time is permitted for the suspension to rebuild its structure, therefore, the term ''apparent yield stress'' was used herein. An ascending sweep was imposed in logarithmically spaced steps (5 points per decade) from $\dot{\gamma} = 1 \times 10^{-3}$ s^{-1} to 200 s^{-1} with a 10 s data-averaging period. The ascending sweep was followed by a descending sweep over the same shear rate range.

• The viscoelastic behavior and elasticity of aggregates in the suspensions were characterized *via* small amplitude oscillatory (SAOS) rheometry. Following the shear flow experiment, a shear-strain amplitude (γ) sweep from $\gamma = 0.001\%$ to 1000% was performed, at a fixed frequency of 1 Hz.

It should be noted that the rheological properties of portlandite suspensions were not affected by potential carbonation of $Ca(OH)_2$ particles (*i.e.*, the reaction of portlandite with atmospheric CO_2 to produce solid calcium carbonates) over the course of rheology measurements. The initial purity of $Ca(OH)_2$ used herein was as high as 95% (very pure), and this amount did not change over the course of the rheology experiment undertaken in atmospheric conditions ($[CO_2] = 0.04\%$). This was verified by comparing the carbonation extents of portlandite before and after rheology measurements using thermogravimetric analysis (TGA; STA 6000, PerkinElmer). Since portlandite can rapidly carbonate in its near-surface vicinity (*i.e.*, the first few nanometers), TGA cannot offer

definitive evidence that no surface carbonation occurred. Nevertheless, however, the behavior of the portlandite suspensions was clearly distinguished from that of calcite suspensions (not shown). More importantly, the portlandite particles did not show differing atom density differences, *i.e.*, at the near surface, and particle interior when observed in backscatter imaging mode, or in the transmission electron microscope. This collective of evidence suggests that the portlandite particles were not affected by (surficial) carbonation.

Polymer adsorption. The extent of polymer adsorption onto portlandite surfaces was determined using a total organic carbon (TOC) analyzer (Shimadzu, TOC-L). Here, suspensions of $\phi = 0.05$ with varying dispersant dosages up to 5% by mass of solids (*i.e.*, an upper bound on dosage for typical applications) were composed and allowed to equilibrate for 24 h. Following equilibration, the suspensions were then centrifuged for 15 min at 4696 rpm, and the supernatant was removed and filtered using a 0.20 μm syringe filter. With all solid particles removed, the amount of non-adsorbed polymer present was measured by TOC analysis. As the inorganic carbon content may be elevated due to the formation of calcium carbonate ($CaCO_3$), a non-purgeable organic carbon (NPOC) analysis was performed. Since the carbon content of each of the dispersants was unknown, a calibration for each of the three dispersants was also established by testing a series of known dilutions of dispersant up to a maximum dosage equivalent to that found in the adsorption experiments. This allowed for a direct conversion to be made between the NPOC content and dispersant dosage, which was unique for each dispersant. The extent of polymer adsorption was then calculated using a mass balance with the original amount of polymer added.

Dynamic light scattering. To assess the aggregation kinetics of suspensions for varying dispersant types and dosages, dynamic light scattering (DLS) analysis (Malvern, Zetasizer Nano) was carried out over time. Using dilute suspensions (0.05 g_{solid} $L_{solution}^{-1}$) of portlandite in water, the *Z*-average size (intensity-based overall average size) of particle aggregates was determined by cumulants analysis (Malvern, Zetasizer Software). Each measurement was taken at around 5 min intervals for up to 1 h with individual measurements requiring about 2 min each.

3. Results and discussion

3.1. Aggregation, jamming, and yielding of portlandite suspensions

Portlandite particles suspended in a self-saturated or native solution (pH = 12.6) feature a zeta potential of $\zeta = +34$ mV (see Fig. 1a). Typically, this magnitude of zeta potential is sufficient to impart electrostatic stability to a suspension.[45] However, electrostatic repulsion alone is unable to prevent particle aggregation and produce stable suspensions of portlandite. As such, portlandite suspensions demonstrated yield stresses that increase sharply with ϕ (see Fig. 1b) and a maximum achievable particle loading of $\phi_{max} \approx 0.36$. The ϕ_{max} was determined by fitting the yield stress-ϕ trends by a power-law function of the form $\sigma_y = (\phi_j - \phi)^m$,[46] where ϕ_j is the jamming volume fraction (analogous to ϕ_{max} in Krieger–Dougherty equation)[47] and m is a fitting exponent (see Fig. 1b). It must be noted here that while suspensions of particles that offer long-range repulsion can exhibit significant yield stresses at low particle loading (*e.g.*, in suspensions comprising particles with thick adsorbed/grafted polymer layers that result in an expanded excluded volume around the particles),[15,48] the portlandite suspensions considered herein showed a high tendency for aggregation, which produced sharply increasing yield stresses, as discussed below.

An examination of the interparticle interactions reveals why, despite their high zeta potentials, portlandite suspensions are unstable. The (symmetric) interparticle interaction potential (V) between portlandite particles as a function of distance from the particle surface x (eqn (1)) includes the contributions of electrostatic repulsion (V_{es}) that can be modeled using the Hogg–Healy–Fuerstenau[49] solution to the Poisson–Boltzmann equation, and

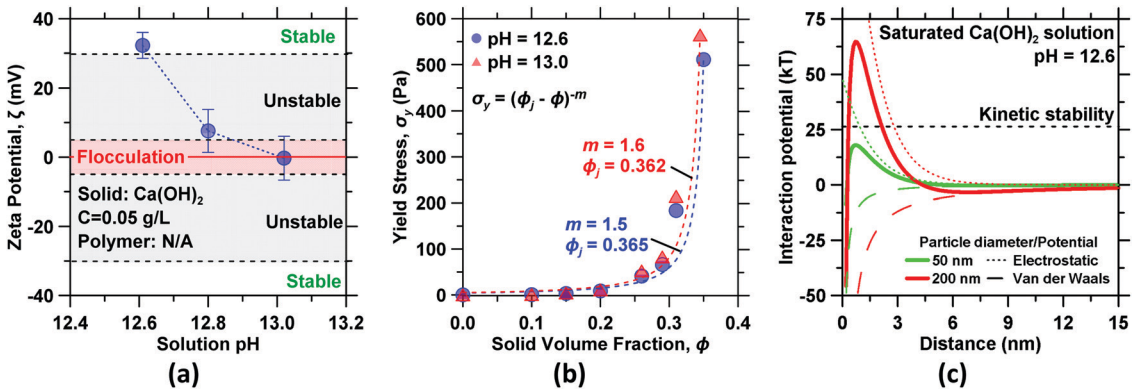

Fig. 1 (a) Zeta potential ζ of $Ca(OH)_2$ particles as a function of pH in a saturated $Ca(OH)_2$ solution based on three replicate measurements. pH adjustments, as needed, were carried out by titrating with NaOH. The stable, unstable, and flocculation regions are included as reported elsewhere.[54,55] (b) $Ca(OH)_2$ suspension's yield stress σ_y as a function of solid volume fraction ϕ at native pH (circles) and at the IEP (triangles) in the absence of any dispersant. Here, based on three replicate measurements, an uncertainty of 9% in the yield stress and 5% in fitting parameters was observed. The dashed lines indicate fits to the data with a power-law function of the form $\sigma_y = (\phi_j - \phi)^m$, where ϕ_j is the jamming volume fraction. (c) The calculated interparticle potentials based on electrostatic and van der Waals interactions for $Ca(OH)_2$ particles suspended in a saturated $Ca(OH)_2$ solution (pH 12.6).

van der Waals attraction (V_{vdW}), calculated using the nonretarded Hamaker pair potentials.[50,51]

$$V(x) = V_{es}(x) + V_{vdW}(x) = \pi\varepsilon_r\varepsilon_0\psi^2 R\ln[1+\exp(-\kappa x)] - \frac{AR}{12x} \quad (1)$$

Here, ε_r and ε_0 are the relative permittivity and permittivity of free space, respectively, and R is particle radius. The characteristic electrostatic decay length, or Debye length κ^{-1} was estimated as $\kappa^{-1} = \sqrt{\varepsilon_r\varepsilon_0 kT/2e^2I}$, with k, T and e being the Boltzmann constant, temperature, and the elementary charge, respectively, and I being the ionic strength of the medium defined as $0.5\sum c_i z_i^2$ with c_i and z_i being the molar concentration and the valence of each ionic species present in the solution. For $Ca(OH)_2$ suspensions at their natural pH = 12.6, the ionic strength is 60.9 mM, resulting in a Debye length κ^{-1} = 1.2 nm. The surface potential ψ was estimated from the measured zeta potential (ζ) of the particles at the shear plane ($x_s \sim \kappa^{-1}$)[52] as $\psi = \zeta\exp(\kappa x_s)$. The Hamaker constant $A = 2.2 \times 10^{-20}$ J for $Ca(OH)_2$ was calculated following Lifshitz theory (see ESI,† Section B, eqn (S1)).[53]

Fig. 1c shows the total interparticle interaction potentials as well as the contributions from electrostatic and van der Waals interactions for 50 nm and 200 nm diameter portlandite particles. Strong screening of electrostatic interactions resulting from the compression of the electric double layer (EDL) that arises from the high ionic strength produces electrostatic repulsions for distances $x \lesssim 5$ nm. Short range van der Waals attraction dominates interparticle interactions at distances $x \lesssim 0.5$ nm. The resulting net interparticle interaction therefore transitions from a strong van der Waals attraction at 0.5 nm to an electrostatic repulsion in the range of 0.5 nm $\lesssim x \lesssim$ 5 nm with a maximum around $x \sim 0.7$ nm and a weak van der Waals attraction for $x > 5$ nm, independent of particle size. The magnitude of the repulsive maximum is critical in determining the suspension's stability. The minimum energy of the repulsive barrier to prevent particle aggregation over a timescale τ can be estimated as $E_{min} = kT\ln(\tau f_c)$, where f_c is the collision frequency of particles under the influence of thermal forces (see ESI,† Section C).[53] The kinetic criterion to maintain suspension stability over 24 h corresponds to $E_{min} = 25kT \pm 3kT$ for particles with a size on the order of 50 nm to 200 nm, as indicated by the horizontal dashed line in Fig. 1c. In general, for portlandite particles smaller than 65 nm, the strength of the repulsive potential was found to be smaller than the kinetic barrier across all interparticle separations while for particles larger than 65 nm, interparticle repulsion was found to restrict interparticle approach only within distances smaller than ~3 nm. Thus, although the measured zeta potential of ζ = +34 mV at pH = 12.6 is relatively high, high concentrations of counterions in the solution compress the EDL around the particles, thereby screening electrostatic repulsions very effectively. Consequently, the smaller primary portlandite particles (<65 nm) are predicted to be unstable, and the larger particles (<200 nm) are only stable at very small interparticle spacings. Therefore, aggregation of portlandite particles for particle sizes <200 nm is assured to occur, thereby compromising the suspension's stability.

On account of their electrokinetic instability and tendency to aggregate, portlandite suspensions display a sharp rise in yield stress at moderate particle loadings (ϕ = 0.2; Fig. 1b). As such, solid volume fractions above ϕ_{max} = 0.36 (see Fig. 1b) were inaccessible in these portlandite suspensions that have polydisperse plate-like particles in high ionic strength aqueous environment. This is far inferior to the maximum achievable packing fraction, *e.g.* of random close packings of monodisperse spheres (ϕ_{rcp} = 0.638). Furthermore, the yielding behavior of native suspensions (pH = 12.6) was largely analogous to the suspensions with their pH regulated to the isoelectric point (IEP, pH_{IEP} = 13; Fig. 1a), resulting in nearly identical ϕ_{max} (see Fig. 1b). At the IEP, electrostatic interactions between the particles are entirely screened and only (attractive) van der Waals interactions operate, maximizing aggregation. The similarity of the yield stress trends between the native portlandite suspensions and portlandite suspensions at IEP with maximal aggregation indicates that particle aggregation is nearly maximized at pH 12.6. Significantly, these observations confirm that zeta potentials cannot be used as an indicator of stability for suspensions comprising strongly charged particles that generate high concentrations of solubilized counterions. It should further be pointed out that changing (reducing) the solution pH to increase the zeta potential of the particles is ineffective for $Ca(OH)_2$ particulates, as on account of their solubility and dissolution they self-regulate the pH of their local environment. It is especially for these reasons that dispersant-induced interactions are critical to control the rheology of portlandite (and other charged, soluble particle) suspensions.

3.2. Influences of dispersants on stability and rheology of portlandite suspensions

Fig. 2 displays the effects of dispersant addition for three dispersants including: a polyacrylic acid-based linear polyelectrolyte dispersant (PAA), a lignosulfonate dispersant (LS), and a polycarboxylate ether-based comb polyelectrolyte dispersant (PCE) composed of a polyacrylic acid backbone and polyethylene glycol sidechains on the behavior of $Ca(OH)_2$ suspensions. The impact of dispersant on the suspension yield stress was found to vary significantly with dispersant type (see Fig. 2a). For example, at a constant solid volume fraction (ϕ = 0.35), a remarkable 10^5-fold decrease in yield stress was achieved at a PCE dosage of 1.5 mass% (polymer/solid). The reduction of the yield stress was found to increase exponentially with increasing dispersant dosage ρ (% of solid); $\sigma_y/\sigma_{y,0} = \exp(-B\rho)$ where $\sigma_{y,0}$ = 663 Pa (yield stress of the ϕ = 0.35 portlandite suspension with no dispersant). Here, B denotes the efficiency of the dispersant in reducing the suspension yield stress; the effect of B_{PCE} = 5.74 in an exponential function far exceeds those of B_{PAA} = 2.06 and B_{LS} = 1.13. The length scale and strength of electrosteric repulsions provided by comb-like dispersants depend on the thickness of the adsorbed layer, which in turn is dictated by the length, charge density, and stiffness of the polyelectrolyte chain as well as the strength of the attractive electrostatic interactions between the polyelectrolyte and the particles.[14,39,56] Introduction of neutral side chains to the polyelectrolyte backbone further enhances the efficacy of the dispersants.[16,17,57] The neutral side

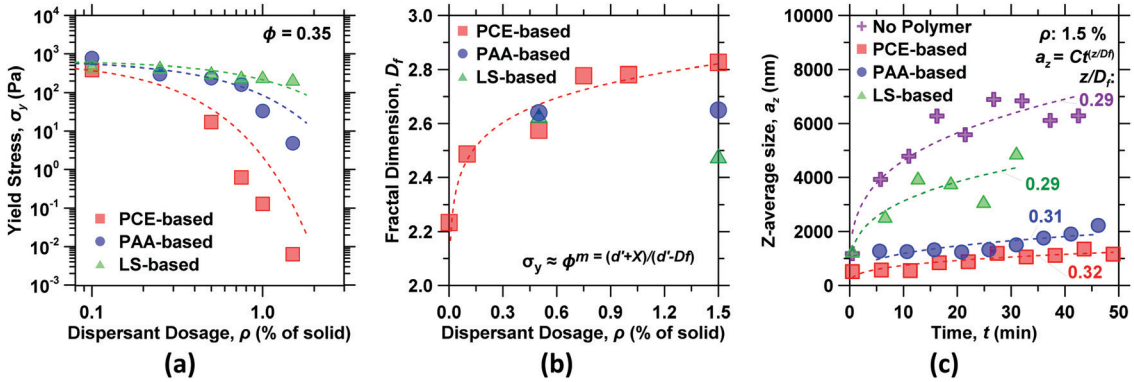

Fig. 2 (a) The apparent yield stress of $Ca(OH)_2$ suspensions σ_y as a function of dispersant dosage ρ for the three types of dispersants for $\phi = 0.35$. Here, based on 3 replicate measurements, the highest uncertainty of 9% in the yield stress was observed. The dashed lines indicate exponential function fits to the data of the form $\sigma_y = \sigma_{y,0}\exp(-B\rho)$, with $\sigma_{y,0}$ and B being the yield stress of suspension without dispersants and a fitting parameter, respectively. (b) Fractal dimension D_f calculated from power-law scaling of yield stress *vs.* solid volume fraction for portlandite suspensions with various dispersant dosages and types. (c) The "Z-average" size of $Ca(OH)_2$ aggregates as determined by DLS in suspensions composed at $\phi = 0.002$. These values are indicative of floc size; as $Ca(OH)_2$ particles aggregate, the Z-average size increases. Based on 5 replicate measurements, the highest uncertainty of 20% in the Z-average particle size was observed. The dashed lines indicate fits of the form $a_z = Ct^{z/D_f}$ to the data, where C and z are fitting parameters.

chains in such 'comb' polyelectrolytes stretch out yet further away from the particle's surface into the solvent, leading to higher particle dispersion.

Correspondent with a reduction in the yield stress with dispersant dosage at a fixed particle loading, the incorporation of dispersants also enhanced the maximum achievable particle volume fraction in the suspensions (see ESI,† Fig. S3). This enhancement is best shown by the addition of PCE to portlandite suspensions, wherein ϕ_{max} increased 1.4 times from 0.36 to 0.50 at a PCE dosage $\rho = 1.5\%$ of the solid mass (see ESI,† Fig. S3). The effects of PCE addition on the yield behavior of suspensions were examined over a range of volume fractions (see ESI,† Fig. S3). In the range of $0.1 < \phi < 0.5$, the addition of even modest amounts of PCE led to marked reductions in the yield stress. The influence of adding dispersants could further be quantified by deducing the fractal dimension of the flocs forming in the suspensions (see Fig. 2b). The fractal dimension D_f was extracted from power-law fits of the form $\sigma_y \sim \phi_s^m$ where $m = \frac{D+X}{D-D_f}$. Here, D is the Euclidean dimension (3, for a 3D space), D_f is the fractal dimension of particle clusters, and X is the fractal dimension of the cluster backbones, taken as 1 indicative of a backbone that's not capable of elastic stress transmission (see ESI,† Sections E and F).[58] The yield stress σ_y of the portlandite suspension with no dispersant indicated a power-law scaling $m \approx 5.2$ (see ESI,† Fig. S3), consistent with the observed yield stress behavior of aggregating suspensions of mineral particles.[59] A steady increase in the fractal dimension (*i.e.*, approaching 3 for a sphere) of the suspensions with PCE dosage (see Fig. 2b) signified that suspension structure shifts further away from the diffusion-limited aggregation regime on account of enhanced steric barriers that retard aggregation upon addition of PCE to the suspensions. This results in a structural transition from more branched flocs (*i.e.*, more open structure) to either denser flocs or greater particle dispersion. This transition occurs when the forces mitigating aggregation grow greater and particle sticking/collision efficiency resulting from diffusing clusters decreases. This permits an increase in the maximum achievable particle volume fraction. It should be noted that depending on the suspension structure, the increase in the value of the fractal dimension can be an indicative of two different cases: (i) individual flocs are approaching more ideal packing into a spherical shape, which can be accomplished by forming more densely-packed flocs, or (ii) stronger particle dispersion, whereby flocs are made up of few primary particles.[58,60] As the reduction in yield stress is much greater for suspensions made with the comb-like dispersant, it is inferred that any flocs formed in these suspensions are much smaller with weaker linkages than that of the native portlandite suspension and those made with linear dispersants (see ESI,† Fig. S4).

The reduction in yield stress upon the addition of the dispersants corresponds to restricted aggregate sizes and retarded aggregate growth. The temporal evolution of aggregate size using dynamic light scattering measurements in very dilute portlandite suspensions highlighted the close correlation between the efficacy of dispersants in reducing yield stress and inhibiting aggregate growth. In general, the addition of PCE, which most reduced yield stresses, resulted in the smallest and slowest-growing $Ca(OH)_2$ aggregates. Whereas the addition of LS, which resulted in only marginally smaller suspensions yield stresses, led to only minor reductions in both aggregate sizes and growth rates as compared to the native $Ca(OH)_2$ suspension (see Fig. 2c). Although the size evolution of PCE and PAA was similar, the marked difference in the effect on yield stress results from the greater ability of PCE to provide a steric barrier between particles. While both dispersants are effective at reducing the overall size of aggregates, PAA does not keep the smaller aggregates spaced apart, leading to smaller interparticle spacing and higher rheological properties. The addition of dispersants also led to weaker aggregates, such that the reduction of suspension yield stress with dispersant type and dosage correlated closely with lower strains and the energy required to disrupt the overall suspension's structure (see ESI,† Fig. S4). Despite similar floc size for PCE and PAA dispersants,

weaker linkages between flocs/aggregates were noted for the comb polyelectrolyte PCE dispersant due to its steric hindrance.

The elucidation of aggregate growth kinetics enables further insights into the nature of the aggregation processes. The mean aggregate size a_z for aggregates should grow with time t as $a_z = Ct^{z/D_f}$, where C is a numerical prefactor and z is related to the nature of the aggregation processes. For diffusion limited aggregation, $z = 1$ and $D_f = 1.75$–1.8, resulting in $a_z \sim t^{0.55}$. For reaction limited aggregates, $D_f \geq 2.1$ and z is generally smaller than 1, resulting in the temporal power-law exponent (z/D_f) generally being <0.45.[61] The temporal power-law exponent of aggregate growth in $Ca(OH)_2$ suspensions, both with and without dispersants, was found to be smaller than 0.4, pointing towards reaction limited aggregation of $Ca(OH)_2$ particles. Using D_f data from Fig. 2b, z values were determined to be smaller than 1 ($z_{none} = 0.65$, $z_{LS} = 0.72$, $z_{PAA} = 0.82$, and $z_{PCE} = 0.91$), highlighting the prominent contribution of the sticking of smaller clusters in the aggregation process.[61] The values of C ($C_{none} = 2372$, $C_{LS} = 1593$, $C_{PAA} = 582$, and $C_{PCE} = 355$) corresponded to the effectiveness of each dispersant in reducing aggregation in the suspensions and correlated well with the fitting parameter B (see Fig. 2a), highlighting the reduced propensity towards aggregation induced by the addition of dispersants. To further analyze the aggregation kinetics *via* Smoluchowski's model,[62] the floc size evolution in Fig. 2c was used to assess the rate of increase in the number of particles N_i in time t within a floc by $N_i \approx \left(\frac{R_{floc_i}}{a}\right)^{D_f}$,[63] where R_{floc_i} is the floc size at time t (using data from Fig. 2c) and a is the primary particle size. The aggregation rate constant *via* colliding particles with time k_a was determined by fitting the N_i/N_0-time trends by a linear function of the form $N_i/N_0 = k_a t$. The normalized particle number N_i/N_0 within floc was obtained by particle number N_i at time t to its initial reading N_0. The k_a values were found to be substantially smaller than that the neat portlandite suspension ($k_{a,none} = 0.023\ s^{-1}$, $k_{a,LS} = 0.013\ s^{-1}$, $k_{a,PAA} = 0.006\ s^{-1}$, and $k_{a,PCE} = 0.004\ s^{-1}$). This reveals that the addition of dispersant, especially PCE, significantly reduces particle sticking and collision efficiency as well as retards aggregation growth greatly. Herein, it should be noted that the solvent's viscosity increases only marginally, owing to the presence of non-adsorbed dispersant in the solvent. As such, the reduced rate of aggregation for suspensions with dispersant is not due to reduced particle collisions, *e.g.*, arising from possible increases in solvent viscosity, but due to the increased inter-particle repulsions that are induced by the dispersant. It should be noted that the free dispersant in the solvent may have other impacts such as attractive depletion in addition to altering solvent viscosity. However, the contribution of attraction depletion to particle bridging/flocculation and the consequent change (increase) in rheological properties of suspension is expected to be marginal due to the relatively low molecular weights of the backbone of dispersants investigated herein. As the floc size for suspensions made with dispersants at the highest dosage ($\rho = 1.5\%$ of the solid mass) remained smaller than that of the native portlandite suspension (as evidenced by DLS data in Fig. 2c), it is inferred that free dispersant in solvent does not result in polymer bridging induced flocculation of particles.

A quantification of dispersant adsorption on particle surfaces was pursued to link the dispersant affinity to the observed yield stress reductions. The relationship between the amount of adsorbed dispersant, ρ_a, and free dispersant, ρ_f, is depicted in Fig. 3a and was described by a Langmuir adsorption isotherm of the form: $\frac{\rho_a}{\rho_{a,m}} = \frac{\rho_f K}{1 + \rho_f K}$.[54,64] A plateau in the amount of adsorbed dispersant $\rho_{a,m}$ with increasing ρ_f was recognized and the equilibrium constant K, which describes the ease and tendency of polymer adsorption onto the portlandite surfaces, was obtained (Table 1). It should be noted that (i) adsorption behavior was only examined in a range that is expected to be

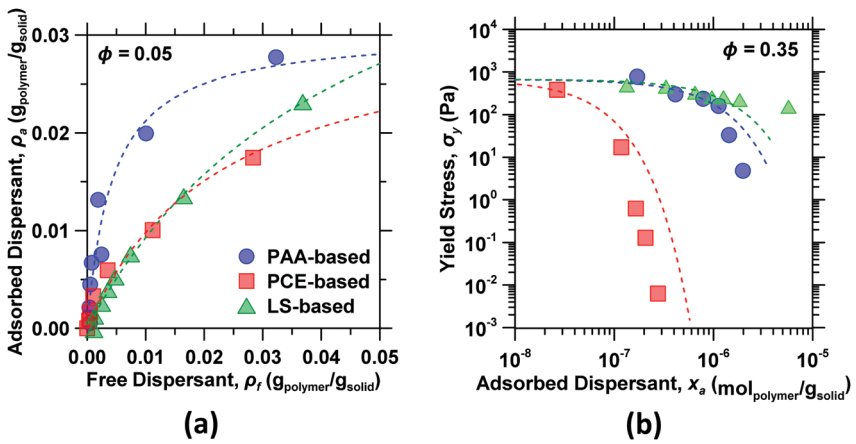

Fig. 3 (a) The amount of dispersant adsorbed onto portlandite particles surfaces ρ_a as a function of the free dispersant concentration in solution ρ_f. The dashed lines indicate fits to the data with a Langmuir expression for monolayer adsorption. (b) The yield stress σ_y of portlandite suspensions as a function of the moles of dispersant adsorbed on the particle surfaces per unit mass of the solids x_a. The dashed lines indicate exponential function fits to the data of the form $\sigma_y = \sigma_{y,0}\exp(-Dx_a)$, where $\sigma_{y,0} = 663$ Pa (yield stress of the $\phi = 0.35$ portlandite suspension with no dispersant) and D is a fitting parameter. Here, based on 5 replicates, the highest uncertainty of 10% in the amount of dispersant adsorbed, was noted.

relevant for typical applications, *i.e.*, $\rho \leq 5\%$ [*N.B.*: it is important to limit the dispersant dosages to restrict the abundance of free polymer in solution, which could otherwise induce substantial attractive depletion forces], and (ii) the assumption in the Langmuir adsorption model of on-average monolayer adsorption is expected to be reasonable for the dosages considered herein although multilayer adsorption may occur at higher dispersant concentrations.[14,21,65]

The polymer charge density, molecular weight, and length of side chains all contribute towards the binding affinity K, where higher charge densities, larger molecular weights, and smaller persistence lengths should result in higher values of K. The linear and densely charged PAA dispersants adsorbed readily onto the particle surfaces, providing steric exclusion to the particles while retaining high adsorption. The lower binding affinity of the LS chains is hypothesized to result from the aromatic rings within its structure, which reduces its flexibility, thus entropically limiting adsorption due to the lack of favorable conformations. The lower binding affinity of PCE chains can be attributed to the specific molecular structure. Even though the PCE has the largest molecular weight amongst all the three dispersants ($\sim$39.5 kDa), a majority of it ($\sim$32.5 kDa) is contributed by the neutral polyethylene glycol sidechains (see ESI,† Section H). The polyacrylic acid backbone accounts for around 7 kDa of the total molecular weight and is expected to be $\sim$50% less charge dense than linear PAA chains. The presence of side chains would also reduce the conformational entropy of the PCE chains. The combined impact of lower charge density and conformation entropy of the polyacrylic acid backbone on adsorption translates to a significant decrease in the binding affinity of the PCE chains.[21,66]

The efficacy of the dispersants is highlighted by examining the yield stress reductions plotted as a function of the mole fraction of adsorbed dispersant (see Fig. 3b). When normalized by mole fraction, the difference in the efficacies of PCE and other dispersants in reducing the yield stress becomes even more drastic. In effect, even with low binding affinity and at very small dosages, the polyethylene glycol side chains of the adsorbed PCE polymers stretch into the solvent and provide strong screening of the attractive van der Waals forces. The linear PAA and LS dispersants show similar behavior at low levels of adsorption, forming an adsorbed layer on the surface whose thickness increases with increasing polymer content. LS shows a saturation in affecting yield behavior while the effectiveness of PAA improves above an adsorption level around 10^{-6} $mol_{polymer}$ g_{solid}^{-1}. This can be attributed to a sharp increase in the dispersant layer thickness after the particle surfaces are saturated with polymer, owing to the higher PAA charge density. The marked difference in the effectiveness of linear and comb polyelectrolyte dispersants, however, highlights the role of side chains in providing an effective steric barrier to particle aggregation. Furthermore, while larger linear polyelectrolytes facilitate aggregation due to overlap of the adsorbed polyelectrolyte layers and resulting particle bridging,[67,68] increasing the molecular weight of comb polyelectrolytes in fact facilitates dispersion. This is due to the increased adsorbed polymer layer thickness, owing to the enhanced steric repulsion between the overlapping neutral sidechains.

The influence of the dispersants on altering interparticle separations was assessed, to a first approximation, by estimating the average surface-to-surface separation amongst particles based on knowledge of their solid volume fraction in the suspension and the particle size distribution (see ESI,† Section D). Fig. 4a shows a simplified trace for the native portlandite suspension's yield stress as a function of the interparticle spacing d_p for a range of particle volume fractions; $0.10 \leq \phi \leq 0.35$. This relationship offers a simple means to establish the correlation between changes in the yield stress σ_y and the average interparticle spacing d_p. This correlation was used to map the effective increase in the interparticle distance that is produced by the addition of dispersants (see Fig. 4a). The outcomes of this analysis, plotted as $|\Delta d_p/\Delta\sigma_y|$ as a function of the amount of adsorbed polymer ρ_a in Fig. 4b, indicate that the differing ability of the dispersants to reduce the suspension's yield stress is intrinsically related to their ability to induce

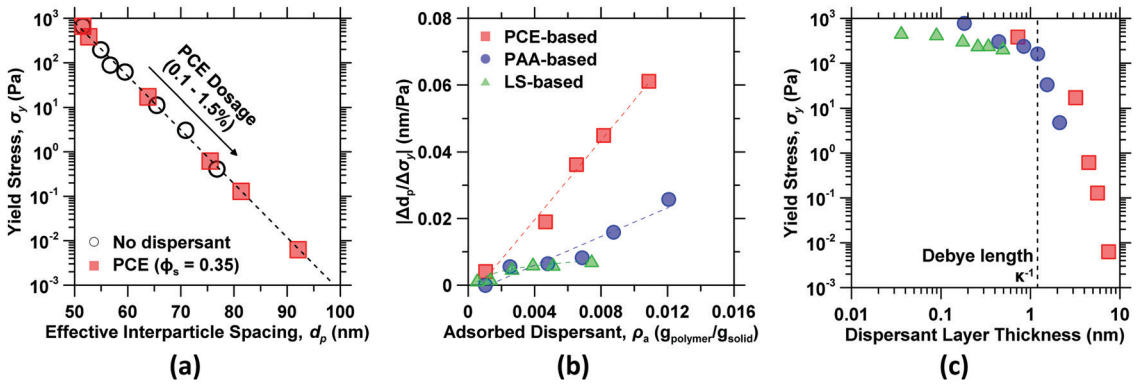

Fig. 4 (a) The suspension's yield stress σ_y as a function of interparticle (surface-to-surface) separation d_p for the native portlandite suspension. By mapping the measured yield stress to the interparticle spacing, the effect of a given dispersant on reducing the yield stress at a specific dosage can be established. (b) Continuation of analysis in (a) showing the reduction in yield stress as the effective interparticle spacing increases for the different polymers. (c) The apparent yield stress as a function of an effective dispersant layer thickness for all the polymers. In general, it is seen that the yield stress reduces by nearly 5 orders of magnitude as the dispersant layer thickness progressively exceeds the electrostatic screening length.

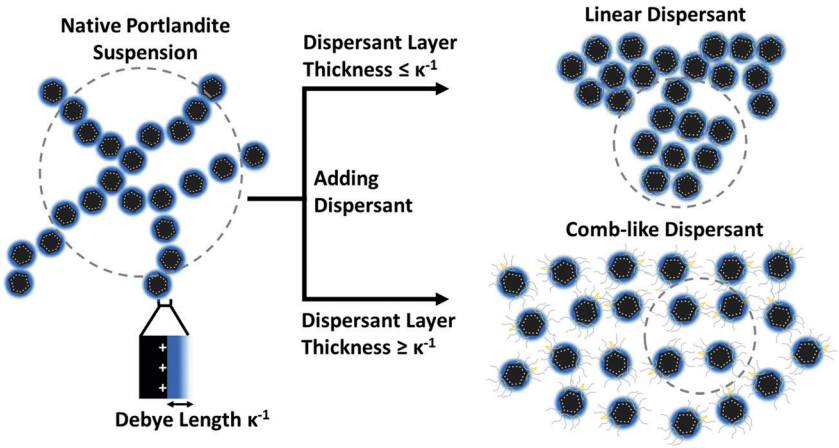

Fig. 5 A schematic illustrating the differences produced in the interparticle spacing and fractal structuring in portlandite suspensions with thin or thick adsorbed layers, corresponding to the addition of linear or comb polyelectrolyte dispersants, respectively. When the dispersant layer thickness exceeds the Debye length (*i.e.*, electrostatic screening length), superior interparticle separations are created *via* steric hindrance effects, leading to effective particle dispersion. The dashed circles indicate fractal flocs.

controllable separations between particles as a function of their adsorption behavior.

The ability to induce controlled interparticle separations is a function of electrosteric behavior, especially in high ionic strength suspensions. A relevant attribute of dispersant in such cases is its hydrodynamic radius (r_H, see Table 1). The hydrodynamic radius describes the physical size of a polymer molecule in a solution. Although r_H does not perfectly describe the conformation of the adsorbed polymer, it offers an estimate of the interaction distance for steric repulsion of each dispersant. Thus, the effectiveness of each dispersant, *i.e.*, the dispersant layer thickness, can be described by the product of its fractional amount adsorbed (*i.e.*, surface coverage, $\rho_a/\rho_{a,m}$) and its hydrodynamic radius. Fig. 4c reveals a remarkable mapping between suspension yield stresses and estimated dispersant layer thickness ($r_H\rho_a/\rho_{a,m}$), with data for all three dispersants collapsing onto a single ''master'' curve. In addition, it is noted that a sharp reduction of nearly five orders of magnitude in the yield stress is produced when the dispersant layer thickness exceeds the electrostatic screening length (*i.e.*, Debye length, κ^{-1}). This observation indicates that, in general, the most prominent attribute of a dispersant is to offer a sufficient dispersant layer thickness that induces physical separation amongst particles over a length scale greater than that over which coulombic forces would operate, as schematically illustrated in Fig. 5. The interparticle interactions produced by adsorbed polymers are controlled by their structure. Since the LS and PAA dispersants do not feature branched or grafted side chains, they cannot present sufficiently thick adsorbed layers, and consequently, do not impose significant interparticle steric repulsion. Furthermore, we acknowledge that r_H for strongly charged polymers (*e.g.*, PAA) will be influenced by chain swelling, owing to intra-chain electrostatic repulsion. Importantly, the swollen conformation should translate to thicker adsorbed polymer layers, again owing to intra-chain repulsion of the non-adsorbed sections of the chains. Taken together, since the PCE is the only dispersant examined herein that is capable of producing a substantial dispersant layer thickness (*e.g.*, as indicated by its comb architecture, high molecular weight, and r_H) that exceeds the electrostatic screening length, it is the only dispersant that is effective at creating larger particle separations, mitigating particle aggregation, and reducing the yield stress of nano- and micro-scale portlandite suspensions.

4. Summary and conclusions

This study has elucidated the impact of polymers that present different dispersion mechanisms (*i.e.*, electrostatic and electrosteric) on the stability and rheological properties of portlandite suspensions that present short screening lengths and a native pH close to the particle's isoelectric point (pH $\approx$ 12.6, IEP: pH $\approx$ 13). Special attention was paid to link the characteristics of dispersants to the suspension's yield behavior. High ionic strengths disrupt electrostatic repulsion by screening charges and induce particle aggregation, resulting in a significant increase in yield stress and consequently lowering the maximum achievable solid volume fraction (ϕ_{max}) in native portlandite suspensions. Thus, it was indicated that simple coulombic repulsion alone is insufficient to affect the rheology of native portlandite suspensions. A stronger screening of the interparticle attractive van der Waals forces was introduced *via* longer-range geometrical particle–particle exclusion by adding polyelectrolyte dispersants that adsorb on particle surfaces and provide steric hindrance, limiting particle aggregation. The ability of dispersants to induce interparticle separation was found to be dominantly controlled by the dispersant layer thickness, and how far it extends into the solvent. Specifically, when the (adsorbed) dispersant layer thickness exceeded the electrostatic screening length in high ionic strength solutions, it imparted interparticle separation *via* steric hindrance. Thus, a ''comb'' polyelectrolyte PCE dispersant was nearly 5$\times$ more effective at reducing the yield stress of portlandite suspensions as compared to linear dispersants at similar portlandite

volume fractions. The analyses highlighted that although the total molecular weight (M_w) is an important characteristic that is indicative of dispersant effectiveness, the molecular weight of the side chains and the hydrodynamic radius are in fact more relevant attributes influencing interparticle separations and aggregation. The understanding gained from this study offers broad insights into the design of more effective dispersants for controlling interparticle separations in suspensions that self-regulate their pH and present short electrostatic screening lengths. This knowledge is fundamental to control the rheological behavior and maximum achievable solid volume fraction of dense suspensions to ensure relevant engineering scale-processability.

Conflicts of interest

There are no conflicts to declare.

Acknowledgements

The authors acknowledge financial support for this research from the National Science Foundation (DMREF: 1922167, CMMI: 1562066, CAREER: 1253269), Department of Energy: Office of Fossil Energy *via* the National Energy Technology Laboratory (NETL; DE-FE0029825 and DE-FE0031718), and TRANSCEND: a joint UCLA-NIST Consortium that is funded by its industry and agency partners. This research was conducted in the Laboratory for the Chemistry of Construction Materials (LC^2) and the Electron Microscopy Core Facility at UCLA. The authors gratefully acknowledge the support provided by these laboratories. The authors thank BASF Corporation: Construction Chemicals (Beachwood, Ohio) for their assistance in polymer characterization. The contents of this paper reflect the views and opinions of the authors, who are responsible for the accuracy of the datasets presented herein, and do not reflect the views and/or policies of the funding agencies, nor do the contents constitute a specification, standard or regulation.

References

1 N. Roussel, *Understanding the Rheology of Concrete*, Elsevier, 2011.
2 P. F. G. Banfill, *Proceedings of the 11th international cement chemistry congress*, 2003, vol. 1, pp. 50–62.
3 X. Liu, Y. Huang and J. Yang, *Ceram. Int.*, 2002, **28**, 159–164.
4 S. B. Johnson, D. E. Dunstan and G. V. Franks, *J. Am. Ceram. Soc.*, 2002, **85**, 1699–1705.
5 A. Vintiloiu and J.-C. Leroux, *J. Controlled Release*, 2008, **125**, 179–192.
6 M. Zignani, C. Tabatabay and R. Gurny, *Adv. Drug Delivery Rev.*, 1995, **16**, 51–60.
7 W. Bauer and D. Nötzel, *Ceram. Int.*, 2014, **40**, 4591–4598.
8 S. Mubeen, Y. Jun, J. Lee and E. W. McFarland, *ACS Appl. Mater. Interfaces*, 2016, **8**, 1759–1765.
9 D. Lowke, E. Dini, A. Perrot, D. Weger, C. Gehlen and B. Dillenburger, *Cem. Concr. Res.*, 2018, **112**, 50–65.
10 X. Ren, H. Shao, T. Lin and H. Zheng, *Mater. Des.*, 2016, **101**, 80–87.
11 E. Ruiz-Agudo and C. Rodriguez-Navarro, *Langmuir*, 2010, **26**, 3868–3877.
12 M. Fourmentin, G. Ovarlez, P. Faure, U. Peter, D. Lesueur, D. Daviller and P. Coussot, *Rheol. Acta*, 2015, **54**, 647–656.
13 W. B. Russel, D. A. Saville and W. R. Schowalter, *Colloidal dispersions*, Cambridge University Press, 1991.
14 A. Zingg, F. Winnefeld, L. Holzer, J. Pakusch, S. Becker and L. Gauckler, *J. Colloid Interface Sci.*, 2008, **323**, 301–312.
15 S. Srivastava, J. H. Shin and L. A. Archer, *Soft Matter*, 2012, **8**, 4097–4108.
16 H. Kamiya, Y. Fukuda, Y. Suzuki, M. Tsukada, T. Kakui and M. Naito, *J. Am. Ceram. Soc.*, 1999, **82**, 3407–3412.
17 A. Pettersson, G. Marino, A. Pursiheimo and J. B. Rosenholm, *J. Colloid Interface Sci.*, 2000, **228**, 73–81.
18 Y. Leong, D. V. Boger and D. Parris, *J. Rheol.*, 1991, **35**, 149–165.
19 P. F. Luckham and J. Klein, *J. Chem. Soc., Faraday Trans. 1*, 1984, **80**, 865–878.
20 Y. De Hazan, J. Heinecke, A. Weber and T. Graule, *J. Colloid Interface Sci.*, 2009, **337**, 66–74.
21 G. H. Kirby and J. A. Lewis, *J. Am. Ceram. Soc.*, 2004, **87**, 1643–1652.
22 S. Dean, C.-T. Chen, L. Struble and H. Zhang, *J. ASTM Int.*, 2006, **3**, 12787.
23 M. Mirnezami, L. Restrepo and J. A. Finch, *J. Colloid Interface Sci.*, 2003, **259**, 36–42.
24 T. Sowoidnich, T. Rachowski, C. Rößler, A. Völkel and H.-M. Ludwig, *Cem. Concr. Res.*, 2015, **73**, 42–50.
25 J. Plank and B. Sachsenhauser, *Cem. Concr. Res.*, 2009, **39**, 1–5.
26 R. G. Bates, V. E. Bower and E. R. Smith, *J. Res. Natl. Bur. Stand.*, 1956, **56**, 305–312.
27 T. P. Murphy, E. E. Prepas, J. T. Lim, J. M. Crosby and D. T. Walty, *Lake Reservoir Manage.*, 1990, **6**, 101–108.
28 S. Lim, W. Jeon, J. Lee, K. Lee and N. Kim, *Water Res.*, 2002, **36**, 4177–4184.
29 Q. Chen, Z. Luo, C. Hills, G. Xue and M. Tyrer, *Water Res.*, 2009, **43**, 2605–2614.
30 B. Rosenberg, P. E. Murray and K. Namerow, *Dent. Traumatol.*, 2007, **23**, 26–29.
31 C. Sathorn, P. Parashos and H. Messer, *Int. Endod. J.*, 2007, **40**, 2–10.
32 U. Sjögren, D. Figdor, L. Spångberg and G. Sundqvist, *Int. Endod. J.*, 1991, **24**, 119–125.
33 F. Martínez-Bustos, Y. K. Chang, A. C. Bannwart, M. E. Rodríguez, P. A. Guedes and E. R. Gaiotti, *Cereal Chem.*, 1998, **75**, 796–801.
34 L. Han, Z. Lu, X. Hao, Y. Cheng and L. Li, *J. Texture Stud.*, 2012, **43**, 227–234.
35 C. Rodriguez-Navarro, E. Hansen and W. S. Ginell, *J. Am. Ceram. Soc.*, 1998, **81**, 3032–3034.
36 O. Cazalla, C. Rodriguez-Navarro, E. Sebastian, G. Cultrone and M. J. D. la Torre, *J. Am. Ceram. Soc.*, 2000, **83**, 1070–1076.
37 D. R. Lide, *CRC Handbook of Chemistry and Physics*, CRC Press, 85th edn, 2004.
38 Q. Shen, T. Zhang and M.-F. Zhu, *Colloids Surf., A*, 2008, **320**, 57–60.

39 L. M. Rueschhoff, J. P. Youngblood and R. W. Trice, *J. Am. Ceram. Soc.*, 2016, **99**, 3857–3865.
40 K. Vance, G. Sant and N. Neithalath, *Cem. Concr. Compos.*, 2015, **59**, 38–48.
41 Q. D. Nguyen and D. V. Boger, *Annu. Rev. Fluid Mech.*, 1992, **24**, 47–88.
42 P. R. de Souza Mendes and R. L. Thompson, *Rheol. Acta*, 2013, **52**, 673–694.
43 S. A. Nair, H. Alghamdi, A. Arora, I. Mehdipour, G. Sant and N. Neithalath, *J. Am. Ceram. Soc.*, 2019, **102**, 3951–3964.
44 F. Khalkhal, P. J. Carreau and G. Ausias, *J. Rheol.*, 2011, **55**, 153–175.
45 M. Wiśniewska, *Powder Technol.*, 2010, **198**, 258–266.
46 E. Brown and H. M. Jaeger, *Phys. Rev. Lett.*, 2009, **103**, 086001.
47 I. M. Krieger and T. J. Dougherty, *Trans. Soc. Rheol.*, 1959, **3**, 137–152.
48 A. R. Studart, E. Amstad and L. J. Gauckler, *Langmuir*, 2007, **23**, 1081–1090.
49 R. Hogg, T. W. Healy and D. W. Fuerstenau, *Trans. Faraday Soc.*, 1966, **62**, 1638–1651.
50 H. C. Hamaker, *Physica*, 1937, **4**, 1058–1072.
51 U. Aschauer, O. Burgos-Montes, R. Moreno and P. Bowen, *J. Dispersion Sci. Technol.*, 2011, **32**, 470–479.
52 W. Ding, X. Liu, L. Song, Q. Li, Q. Zhu, H. Zhu, F. Hu, Y. Luo, L. Zhu and H. Li, *Surf. Sci.*, 2015, **632**, 50–59.
53 J. N. Israelachvili, *Intermolecular and Surface Forces*, Academic Press, 2015.
54 K. Yoshioka, E. Tazawa, K. Kawai and T. Enohata, *Cem. Concr. Res.*, 2002, **32**, 1507–1513.
55 S. Hornig and T. Heinze, *Biomacromolecules*, 2008, **9**, 1487–1492.
56 F. Winnefeld, S. Becker, J. Pakusch and T. Götz, *Cem. Concr. Compos.*, 2007, **29**, 251–262.
57 K. Yoshioka, E. Sakai, M. Daimon and A. Kitahara, *J. Am. Ceram. Soc.*, 1997, **80**, 2667–2671.
58 W.-H. Shih, W. Y. Shih, S.-I. Kim, J. Liu and I. A. Aksay, *Phys. Rev. A: At., Mol., Opt. Phys.*, 1990, **42**, 4772–4779.
59 D. V. Boger, *Annu. Rev. Chem. Biomol. Eng.*, 2013, **4**, 239–257.
60 T. Liberto, M. Le Merrer, C. Barentin, M. Bellotto and J. Colombani, *Soft Matter*, 2017, **13**, 2014–2023.
61 L. T. Trinh, A.-L. Kjøniksen, K. Zhu, K. D. Knudsen, S. Volden, W. R. Glomm and B. Nyström, *Colloid Polym. Sci.*, 2009, **287**, 1391.
62 M. Von Smoluchowski, *Phys. Z. Sowjetunion*, 1916, **17**, 557–571.
63 D. B. Genovese, *Adv. Colloid Interface Sci.*, 2012, **171**, 1–16.
64 F. Khalkhal, A. S. Negi, J. Harrison, C. D. Stokes, D. L. Morgan and C. O. Osuji, *Langmuir*, 2018, **34**, 1092–1099.
65 F. Dalas, A. Nonat, S. Pourchet, M. Mosquet, D. Rinaldi and S. Sabio, *Cem. Concr. Res.*, 2015, **67**, 21–30.
66 J. Yoshikawa, J. A. Lewis and B.-W. Chun, *J. Am. Ceram. Soc.*, 2009, **92**, S42–S49.
67 J. Gregory and S. Barany, *Adv. Colloid Interface Sci.*, 2011, **169**, 1–12.
68 M. Kamibayashi, H. Ogura and Y. Otsubo, *J. Colloid Interface Sci.*, 2008, **321**, 294–301.